Int. J. Multiphase Flow Vol. 16, No. 6, pp. 985–1002, 1990
Printed in Great Britain.

0301-9322/90 $3.00 + 0.00

FINITE ELEMENT SOLUTION OF MULTI-DIMENSIONAL TWO-PHASE FLOW THROUGH POROUS MEDIA WITH ARBITRARY HEATING CONDITIONS

V. X. TUNG† and V. K. DHIR

Mechanical, Aerospace and Nuclear Engineering Department, School of Engineering and Applied Science, University of California, Los Angeles, CA 90024, U.S.A.

(*Received* 8 *November* 1989; *in revised form* 19 *June* 1990)

Abstract—Mechanistic models for flow regime transitions and drag forces proposed in an earlier work are employed to predict two-phase flow characteristics in multi-dimensional porous layers. The numerical scheme calls for elimination of velocities in favor of pressure and void fraction. The momentum equations for vapor and liquid then can be reduced to a system of two partial differential equations (PDEs) which must be solved simultaneously for pressure and void fraction.

Solutions are obtained both in two-dimensional cartesian and in axi-symmetric coordinate systems. The porous layers in both cases are composed of regions with different permeabilities. The finite element method is employed by casting the PDEs in their equivalent variational forms. Two classes of boundary conditions (specified pressure and specified fluid fluxes) can be incorporated in the solution. Volumetric heating can be included as a source term. The numerical procedure is thus suitable for a wide variety of geometry and heating conditions. Numerical solutions are also compared with available experimental data.

Key Words: porous media, two-phase flow, volumetric heating, dryout

1. INTRODUCTION

Basic understanding of two-phase flow through porous media is of importance in several nuclear, chemical and geophysical applications. For example, in light water reactors, in-place recovery from a degraded core accident will depend strongly on the rate at which energy can be removed from the core under different conditions. Several experimental and analytical studies on hydrodynamic aspects of two-phase flow through porous media have been reported in recent literature. A summary of these works is given by Schulenberg & Muller (1984) and Tung (1988). It is unfortunate that most of the previous works have been carried out under the idealized condition of one-dimensional homogeneous porous layers, whereas those encountered in actual practice may be composed of regions with widely varying permeabilities and heating conditions.

Recently, multi-dimensional two-phase flow through porous media has received considerable interest over its potential application in the nuclear industry, oil recovery and geothermal energy. Lee (1986) performed an analytical and experimental study of two-dimensional flow of a two-phase mixture through non-heated porous layers. However, the interfacial drag was neglected in his analysis. Such an assumption has been known to generate erroneous results in porous layers with high permeability, as shown by Tutu *et al.* (1983) and Tung & Dhir (1988). Furthermore, the use of a finite difference scheme in Lee's numerical solution limited its usefulness to geometries with rectangular boundaries.

Tsai (1987) measured dryout heat fluxes in axi-symmetric porous layers with partial volumetric heating. He found that dryout heat flux occurs mostly by a mechanism similar to bottom flooding when the heated zone is surrounded by non-heated porous layers. As a consequence, dryout heat fluxes with partial volumetric heating were much higher than the corresponding counter-current flooding limits. His numerical solutions were also obtained by a finite difference scheme without the interfacial drag term. Capillary pressure was included in his solutions through the use of the Leverett function. In Tsai's work, the solutions were obtained with "pseudo stream functions" to include the source terms due to volumetric heating. Such an approach, however, is only applicable

†Present address: Mechanical Engineering Department, California State University, Long Beach, CA 90840, U.S.A.

for a very limited number of cases since such "pseudo stream functions" only exist for certain distributions of volumetric heating in the porous layers.

It should also be pointed out that, due to a lack of information on relative permeabilities, both Lee (1986) and Tsai (1987) resorted to numerical experimentation to match their experimental data. Their numerical solutions are thus further restricted to a limited set of experimental configuration and flow condition. At best, such solutions only serve to illustrate qualitative arguments on data behavior.

Tung (1988) extended the one-dimensional model proposed by Tung & Dhir (1988) to obtain a solution for two-phase flow through heterogeneous porous media. The use of the finite element method (FEM) in his numerical scheme has relaxed the constraint on the type of boundary conditions which could be analyzed. However, the solution was obtained in terms of the stream functions of the two phases. Such an approach fails when a source term arises through volumetric heating of the porous layer since such a source term precludes the representation of velocities by stream functions.

In light of the aforementioned limitations of previous numerical solutions, a different scheme must be found to obtain solutions with as few restrictions as possible. In the present work, the analysis carried out by Tung (1988) has been modified such that solutions are obtained directly in terms of void fractions and pressure. Mechanistic models for various drag forces proposed by Tung & Dhir (1988) were also incorporated in the numerical solution. Solutions obtained with this scheme are then corroborated by comparison with experimental results obtained by Lee (1986) and Tsai (1987). The numerical scheme is based on the FEM. There are several advantages associated with such a scheme:

(i) Since solutions are obtained directly in terms of void fractions and pressure, volumetric heating can be included simply as a source term. Furthermore, an arbitrary distribution can be handled easily by varying the source term for each element while assembling the global forcing function.
(ii) FEM allows the possible existence of several regions of different permeabilities in the domain. This can be accomplished by varying the permeability of each element in the assembly of the global matrices.
(iii) Non-rectangular domains can be readily accommodated by placing one or two sides of the boundary elements along the boundaries.
(iv) Along the exterior boundaries of the domain, two different boundary conditions—specified pressure or fluid fluxes—are permitted by the present scheme. As such, a combination of surface heating and volume heating can be analyzed.

One disadvantage of the present scheme is the difficulty involved in the assembly of the stiffness matrix and the forcing function. However, the effort involved is not exceedingly overwhelming and is incurred only once during code development. Another disadvantage of the scheme is the computation time required to obtain void fractions. Even then, with proper safeguards and data preparation, a fairly quick return can be achieved. In fact, all numerical computations in this work have been performed on a 386-based AT-compatible personal computer with a typical run time of about 1 h for a reasonably fine grid.

2. ANALYSIS

The hydrodynamic model proposed by Tung & Dhir (1988) has been extended in this work to the multi-dimensional case. The analyses performed in this section are based on the following assumptions:

- Steady state.
- Incompressible fluids.
- Isotropic porous medium.
- Negligible capillary pressure.
- Negligible convective terms.
- Saturated fluids when heating is present.

The assumption of incompressible fluids is generally valid as long as the time-averaged pressure does not possess strong gradients. However, the third assumption requires some clarification. By assuming an isotropic medium, one only requires that the permeability at any given point in the domain is independent of directions. This assumption does not exclude the possibility of a domain composed of several regions, each with a different permeability. For the medium size particle under consideration in this work (1.5–10 mm) the capillary pressure and the convective terms are generally overwhelmed by buoyancy and friction. As such, they have been neglected in the present work. The last assumption implies that volumetric heating can be treated as a source term for the gas phase and a sink term for the liquid phase due to evaporation. Under these assumptions, the momentum equations for the two phases can be written as

$$\epsilon \nabla P_G^* = \frac{\epsilon \rho^*}{1-\rho^*}\mathbf{G} + \mathbf{F}_{PG}^* + \mathbf{F}_i^*, \tag{1}$$

$$(1-\epsilon)\nabla P_L^* = \frac{1-\epsilon}{1-\rho^*}\mathbf{G} + \mathbf{F}_{PL}^* - \mathbf{F}_i^* \tag{2}$$

and

$$P_G^* = P_L^* = P^* \tag{3}$$

where ϵ is the void fraction, $\mathbf{G}$ is a unit vector pointing in the direction of gravity and ρ^* is defined as the density ratio between the gas phase and the liquid phase. The first terms on the r.h.s. of [1] and [2] thus represent the effect of buoyancy. The dimensionless forces $\mathbf{F}_{PG}^*$, and $\mathbf{F}_{PL}^*$ and $\mathbf{F}_i^*$ represent the particle–gas drag, the particle–liquid drag and the liquid–gas interfacial drag, respectively, and are given as

$$\mathbf{F}_{PG}^* = -\left(\frac{a^*\mu_G}{\kappa_G'} + \frac{b^*\rho_G|\mathbf{j}_G|}{\eta_G'}\right)\mathbf{j}_G, \tag{4}$$

$$\mathbf{F}_{PL}^* = -\left(\frac{a^*\mu_L}{\kappa_L'} + \frac{b^*\rho_L|\mathbf{j}_L|}{\eta_L'}\right)\mathbf{j}_L \tag{5}$$

and

$$\mathbf{F}_i^* = -\left[\frac{C_v' v_L}{\alpha g D_b^2(1-\rho^*)} + \frac{C_i'(1-\epsilon+\epsilon\rho^*)}{\alpha^2 g D_b(1-\rho^*)}|\mathbf{j}_S|\right]\mathbf{j}_S, \tag{6}$$

where $\mathbf{j}_G$ and $\mathbf{j}_L$ are the gas and liquid superficial velocities while $\mathbf{j}_S$ is the relative velocity between the gas phase and the mixture,

$$\mathbf{j}_S = \frac{1-\epsilon}{\epsilon}\mathbf{j}_G - \mathbf{j}_L. \tag{7}$$

The effects of particle diameter (D_p) and porosity (α) enter the problem through the parameters a^* and b^* which are associated with the viscous term and the inertial term of the particle drag forces and are given by

$$a^* = \frac{150(1-\alpha)^2}{\alpha^3 D_p^2 g(\rho_L - \rho_G)} \quad \text{and} \quad b^* = \frac{1.75(1-\alpha)}{\alpha^3 D_p g(\rho_L - \rho_G)}. \tag{8}$$

The relative permeability multipliers (κ' and η') and drag coefficients (C_v' and C_i') are functions of the void fraction. The actual variation of these functions with the void fraction is given by Tung & Dhir (1988), and a summary of their results can be found in the appendix. The diameter D_b represents the bubble diameter or the lateral dimension of a slug. It is controlled by surface tension and buoyancy and is given by Tung & Dhir (1988) as

$$D_b = 1.35\left[\frac{\sigma}{g(\rho_L - \rho_G)}\right]^{1/2} \tag{9}$$

if the pore space is large enough to accommodate this bubble size. For porous layers composed

of smaller particles, the size of the bubbles will be limited by the pore space and can be given as

$$D_b = \frac{\alpha}{1-\alpha} D_p. \quad [10]$$

Under the assumption of saturated fluids, the continuity equations can be combined with the energy equations to yield the following constraints on [1] and [2]:

$$\nabla \cdot \mathbf{j}_G = \frac{Q}{\rho_G h_{fg}} \stackrel{\text{def}}{=} q_G \quad [11a]$$

and

$$\nabla \cdot \mathbf{j}_L = \frac{-Q}{\rho_L h_{fg}} \stackrel{\text{def}}{=} q_L, \quad [11b]$$

where Q is the rate of volumetric heating. By combining the two momentum equations [1] and [2] one can reduce these to a simpler form:

$$A_1 \nabla P^* = A_2 \mathbf{G} + \mathbf{j}_G \quad [12a]$$

and

$$B_1 \nabla P^* = B_2 \mathbf{G} + \mathbf{j}_L, \quad [12b]$$

where the coefficients (A_1, A_2, B_1 and B_2) are functions of void fractions.

If a void fraction distribution is known, [12a, b] with constraints [11a, b] may be readily solved for the pressure distribution. The difficulty here remains in the selection of an appropriate void fraction distribution such that the two solutions yield the same pressures. In this work, an iterative procedure is employed whereby a void fraction distribution is first assumed. The coefficients (A_1, A_2, B_1 and B_2) can then be evaluated and the two momentum equations [12a, b] are solved simultaneously. The solution thus yields two sets of pressures. Subsequently, these two sets of pressures are used to correct the void fraction distribution and the iterative procedure can be repeated until convergence has been achieved.

2.1. Solution of Momentum Equations

The two momentum equations [12a, b] possess identical forms and constraints. As a result, only the solution of [12a] with constraint [11a] need be examined. Equation [12b] with constraint [11b] can be solved with an identical numerical procedure. For the sake of clarity, the pressure distributions obtained with [12a] and [12b] will subsequently be referred to as $P_A^{*,0}$ and $P_B^{*,0}$, respectively. By taking the divergence of [12a] and substituting the constraint [11a] into the result, one obtains

$$\nabla \cdot (A_1 \nabla P_A^{*,0}) = \nabla \cdot (A_2 \mathbf{G}) + q_G. \quad [13]$$

An excellent overview of the variational principles involved in the FEM is discussed by Hildebrand (1975) and Wylie (1975). Here, it is stated without proof that a solution of [13] corresponds to a stationary point of a functional given by

$$I = \int_V \left(\tfrac{1}{2} A_1 \nabla P_A^{*,0} \cdot \nabla P_A^{*,0} - A_2 \mathbf{G} \cdot \nabla P_A^{*,0} + q_G P_A^{*,0}\right) dV - \int_A P_A^{*,0} (\mathbf{n} \cdot \mathbf{j}_G)\, dA, \quad [14]$$

where $\mathbf{n}$ is the outward normal on the boundaries. A direct substitution of the first integrand into the well-known Euler–Lagrange equation does indeed yield the original partial differential equation (PDE) [13]. It should be noted that, in [14] the volume integral is performed over the whole domain while the surface integral is only performed along the boundaries where *pressures are not specified.* Along these boundaries, one then must specify *normal fluid fluxes.* It can be shown that the stationary point of such a functional must satisfy the following condition along these boundaries:

$$(A_1 \nabla P_A^{*,0} - A_2 \mathbf{G} - \mathbf{j}_G) \cdot \mathbf{n} = 0. \quad [15]$$

A comparison of the above boundary condition with the original PDE [12a] reveals that [15] is automatically satisfied if known normal fluxes of $\mathbf{j}_G$ are employed in the surface integral of [14].

Normal fluxes then can be automatically incorporated as boundary conditions without a conversion to normal pressure gradients. For any given distribution of void fraction, the pressure distribution can thus be obtained by optimizing the functional I with respect to $P_A^{*,0}$. Detailed implementation of the optimization procedure is discussed at length by Segerlind (1976). It is sufficient to note here that linear quadrilateral elements have been employed in this work to reduce computation time in comparison to the use of triangular elements by Tung (1988). It must also be mentioned that the void fraction and coefficients (A_1 and A_2) are assumed constant within each element. Once the two sets of pressures ($P_A^{*,0}$ and $P_B^{*,0}$) have been obtained, superficial velocities can be found by direct substitution of these into [12a, b].

2.2. Void Fraction Correction

In order to reconcile the difference between the two sets of pressures, one must have a scheme to correct existing void fractions. In fact, the most difficult task of the numerical procedure is that of determining a void fraction distribution which will minimize the discrepancy between the two pressures. The first step in this direction is a linearization of the two momentum equations. Again, only [12a] need to be examined with the tacit understanding that the same procedure applies equally well to [12b]. In general, an equation such as [13] can be linearized as

$$\nabla \cdot [A_1 \nabla(\delta P_A^*) + A_1'(\delta\epsilon)\nabla P_A^{*,0}] = \nabla \cdot [A_2'(\delta\epsilon)\mathbf{G}], \tag{16}$$

where A_1' and A_2' are derivatives of A_1 and A_2 with respect to void fractions while δP_A^* and $\delta\epsilon$ are the first variations of P_A^* and ϵ. Equation [16] implies that, for small variations, if the void fraction is perturbed by $\delta\epsilon$ then the pressure distribution is expected to shift δP_A^* from the present solution $P_A^{*,0}$.

In order to obtain this expected change δP_A^*, one must minimize another functional with respect to δP_A^*:

$$J = \int_V [\tfrac{1}{2} A_1 \nabla(\delta P_A^*) \cdot \nabla(\delta P_A^*) + \boldsymbol{\Omega} \cdot \nabla(\delta P_A^*)(\delta\epsilon)]\, \mathrm{d}V, \tag{17}$$

where $\boldsymbol{\Omega}$ is a known vector defined as

$$\boldsymbol{\Omega} \overset{\text{def}}{=} A_1' \nabla P_A^{*,0} - A_2' \mathbf{G}. \tag{18}$$

If N_p and N_e are the number of nodes and the number of elements in the present grid, the result of such an optimization can be given as a system of simultaneous equations

$$[K_A]\{\delta P_A^*\} = [D_A]\{\delta\epsilon\}, \tag{19}$$

where the stiffness matrix $[K_A]$ is a symmetrical $N_p \times N_p$ sparse matrix, $[D_A]$ is a rectangular $N_p \times N_e$ matrix while $\{\delta P_A^*\}$ and $\{\delta\epsilon\}$ are column vectors with N_p and N_e elements, respectively. Then the variation in P_A^* can be related to the variation in void fraction as

$$\{\delta P_A^*\} = [K_A]^{-1}[D_A]\{\delta\epsilon\} \overset{\text{def}}{=} [M_A]\{\delta\epsilon\}, \tag{20}$$

where $[M_A]$ is a rectangular $N_p \times N_e$ matrix. It should be pointed out that there is another equation similar to [20] resulting from the linearization of [12b]. One can thus write

$$\{P_A^* - P_A^{*,0}\} = [M_A]\{\delta\epsilon\} \tag{21}$$

and

$$\{P_B^* - P_B^{*,0}\} = [M_B]\{\delta\epsilon\}. \tag{22}$$

By taking the difference of the above equations, the expected difference of the two pressure distributions corresponding to a variation $\{\delta\epsilon\}$ in void fraction can be given as

$$\{e\} = \{e^0\} + [M]\{\delta\epsilon\}, \tag{23}$$

where

$$e \overset{\text{def}}{=} P_A^* - P_B^*, \tag{24}$$

$$e^0 \overset{\text{def}}{=} P_A^{*,0} - P_B^{*,0} \tag{25}$$

and

$$[M] \overset{\text{def}}{=} [M_A] - [M_B]. \tag{26}$$

The objective here is to minimize the expected difference $\{e\}$ in the two pressure distributions. One can use a least-square fit for this purpose by minimizing the sum of the square of the errors, which is defined as

$$\gamma_1^2 \overset{\text{def}}{=} \{e\}^T\{e\}$$

$$= \{e^0\}^T\{e^0\} + \{e^0\}^T[M]\{\delta\epsilon\} + \{\delta\epsilon\}^T[M]^T\{e^0\} + \{\delta\epsilon\}^T[M]^T[M]\{\delta\epsilon\}. \tag{27}$$

By setting the derivative of γ_1^2 with respect to $\{\delta\epsilon\}$ equal to zero one obtains a set of simultaneous equations for the correction to void fraction which will minimize the expected difference

$$\frac{d\gamma_1^2}{d\{\delta\epsilon\}} = 2[M]^T\{e^0\} + 2[M]^T[M]\{\delta\epsilon\} = 0. \tag{28}$$

Another alternative way of achieving void fraction correction is to minimize the gradients of the expected difference. In fact, this approach is preferable from a physical standpoint since one would naturally want to match the pressure gradients within each element. Using this approach, another error term may be defined as

$$\gamma_2^2 \overset{\text{def}}{=} \int_V \nabla e \cdot \nabla e \, dV. \tag{29}$$

In matrix form, the above error term can be expressed as

$$\gamma_2^2 = \{e\}^T[K]\{e\}, \tag{30}$$

where $[K]$ is a symmetrical $N_p \times N_p$ sparse matrix which can be broken up by LU-decompositions as

$$\gamma_2^2 = \{e\}^T[U]^T[D][U]\{e\}, \tag{31}$$

where $[U]$ is a sparse upper triangular matrix and $[D]$ is a diagonal matrix. By defining

$$\{e_U\} \overset{\text{def}}{=} [U]\{e\}, \tag{32}$$

$$\{e_U^0\} \overset{\text{def}}{=} [U]\{e^0\} \tag{33}$$

and

$$[M_U] \overset{\text{def}}{=} [U][M], \tag{34}$$

the error term can be expressed as

$$\gamma_2^2 = \{e_U^0\}^T[D]\{e_U^0\} + \{e_U^0\}^T[D][M_U]\{\delta\epsilon\} + \{\delta\epsilon\}^T[M_U]^T[D]\{e_U^0\} + \{\delta\epsilon\}^T[M_U]^T[D][M_U]\{\delta\epsilon\}. \tag{35}$$

By minimizing the above error term with respect to void fraction variation one obtains another set of simultaneous equations for void fraction corrections:

$$\frac{d\gamma_2^2}{d\{\delta\epsilon\}} = 2[M_U]^T[D]\{e_U^0\} + 2[M_U]^T[D][M_U]\{\delta\epsilon\} = 0. \tag{36}$$

In this work, both alternatives have been used in calculating void fraction corrections. It was found that they yield basically the same answers. While the second approach appears to be more complicated, computation time is relatively unaffected and it offers more numerical stability than the first choice.

It should be noted that the equations used to correct void fractions are essentially hyperbolic equations. As such, numerical oscillations will occur near any point of discontinuity in permeability, velocity or heating rate. This is a characteristic commonly observed in numerical solutions of hyperbolic equations such as those involving shock waves. The oscillations arise from the fact that a finite number of terms in a numerical solution cannot approximate a discrete jump in any condition. To reduce these numerical oscillations one may include a dissipation term in the PDEs which, in effect, converts them into elliptic equations. In the present case, this purpose can be served by the inclusion of capillary pressures in the momentum equations. However, this requires a thorough understanding of the formation of the porous media at the interface of two different layers. At such an interface, any discontinuity will be physically spread out by the migration of smaller particles into the interstitials of bigger particles. As a result, both porosity and effective particle diameter will vary smoothly across the mathematical interface. Depending on the ratio of the two particle diameters, capillary pressure may or may not be significant at such an interface. A detailed modelling of the interface, however, is beyond the scope of the present work and a different approach has been undertaken here. Since the numerical oscillations are caused by the approximation of a discrete jump by a finite number of terms in the numerical solution, they can be reduced by relaxing the matching condition near the discontinuities. The simplest way to achieve this is to assign a different weighting factor to the elements near the discontinuities while performing the integration in [29]. In doing so, the error term in [29] must be redefined as

$$\gamma_3^2 \overset{\text{def}}{=} \int_V W(x, y, z) \nabla e \cdot \nabla e \, dV, \qquad [37]$$

where the weighting factor $W(x, y, z)$ is unity far away from the discontinuity. Near the discontinuities, one must reduce the weighting factor to reduce overshooting and thus the numerical oscillations. In extreme cases, the weighting factor may have to be reduced to ≈ 0.1–0.2 near the discontinuities. The void fraction correction then can be found as previously described by following [30]–[36].

3. RESULTS AND DISCUSSION

In this section, various geometries and heating conditions are examined using the present numerical procedure. Each set of calculations corresponds to an experimental condition employed in selected studies in the literature.

3.1. Two-dimensional Geometry Without Volumetric Heating

The present numerical scheme has been used to predict the flow pattern in two-dimensional two-phase flow through porous media. The chosen configurations correspond exactly with those employed in Lee's (1986) experiments so that a direct comparison can be made. The two-phase mixture flows through a rectangular channel of width $W = 38$ cm and variable height H, as shown in figure 1. The right half of the channel is obstructed by a thin plate located at 10 cm above the inlet. At the top of the channel, the mixture is discharged into the atmosphere. Consequently, an isobaric boundary condition must be applied at the exit. The porous layers within the channel in Lee's (1986) experiments are formed with particles of two different sizes. Particles of size D_{p_1} occupy the region directly above the blockage while particles of size D_{p_0} occupy the rest of the channel, as shown in figure 1. The superficial velocities of air and water are uniform at the inlet and will be denoted as J_G and J_L in the subsequent discussion.

Solutions obtained for the case $D_{p_0} = D_{p_1} = 6$ mm, $H = 43$ cm, $J_G = 9.75$ mm/s and $J_L = 10.9$ mm/s are shown in figures 2(a, b). The predicted flow velocities are plotted in figure 2(a) for the region above the blockage. As the gas attempts to negotiate the corner imposed by the blockage, the fraction injected on the right-hand side must find the shortest path of escape. Consequently, most of this gas flow is squeezed into a small area near the corner and the gas velocity is highest there. Above the blockage, buoyancy is the main driving force and the gas is

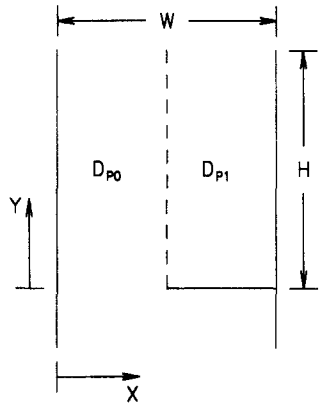

Figure 1. Two-dimensional geometry with a blockage.

driven almost straight up with very little penetration into the right-hand side. As a result, the point of maximum gas velocity remains near the centerline. The liquid, however, displays an entirely different flow pattern. Since most of the gas is flowing through the left-hand side of the centerline, its presence reduces the flow area available for the liquid in this region and the liquid must find

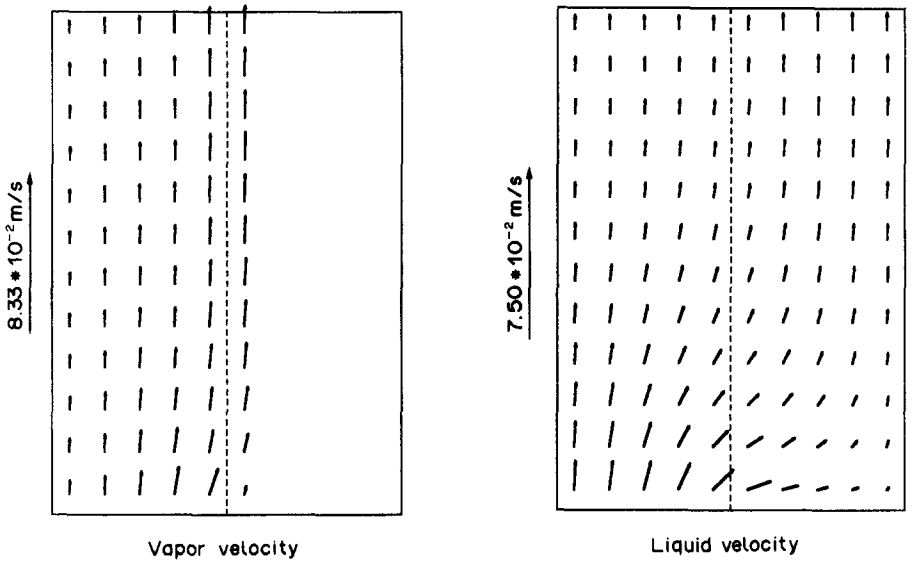

(a)

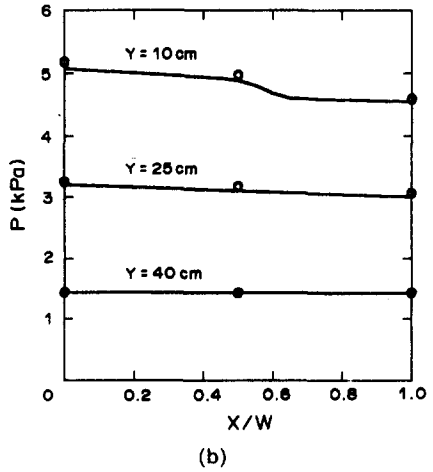

(b)

Figure 2. Two-dimensional solution with uniform particle size.

an alternative flow path with lower resistance. The liquid velocity through the left-hand side is thus slightly smaller than that through the right-hand side of the centerline. The pressure drops obtained by the present numerical scheme at different heights above the blockage are plotted in figure 2(b), along with experimental data obtained by Lee (1986). The solution shows that pressure variation across the channel is greatest near the corner of the blockage. This variation, however, diminishes near the outlet of the channel since an isobaric condition has been applied there. Along the vertical walls, the normal pressure gradient vanishes due to an impermeable boundary condition. It is encouraging to note that the predictions are generally within a few percent of Lee's (1986) data. Measurements of void fractions are not reported in Lee's work for this case, hence a direct comparison cannot be made.

The solutions obtained for the case $D_{P_0} = 6$ mm, $D_{P_1} = 2.5$ mm, $H = 56$ cm, $J_G = 9.75$ mm/s and $J_L = 8.78$ mm/s are shown in figures 3(a–c). The velocities shown in figure 3(a) display a remarkable difference from those shown in figure 2(a). With the presence of a more permeable porous layer on the left-hand side of the domain, most of the gas and liquid flow through this region resulting in higher velocities there. Again the gas velocities show a maximum near the centerline. However, this peak has been shifted slightly to the left of the centerline where permeability is the highest. The predicted pressure drops shown in figure 3(b) again indicate a sharp variation near the corner

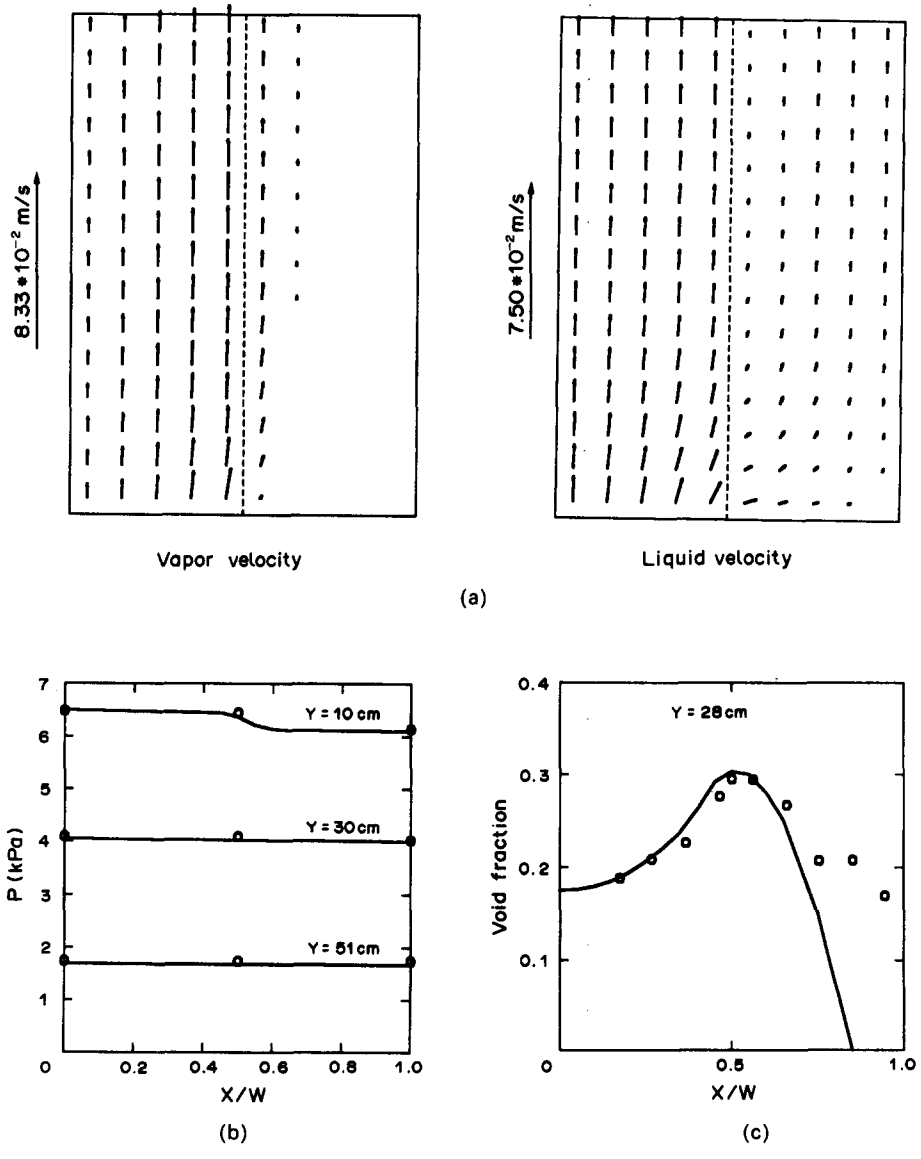

Figure 3. Two-dimensional solution with small particles above the blockage.

of the blockage and remain in fair agreement with Lee's (1986) data. The predicted void fractions are plotted in figure 3(c) along with Lee's data for this particular case. Results indicate that the location of the maximum void fraction occurs near the centerline and coincides with the point of maximum gas velocity. Beyond this maximum, the void fraction decreases very rapidly, indicating that gas velocity in this region is negligible. Void fractions in the region with higher gas velocity are in good agreement with Lee's data. However, the present model tends to underpredict the void fractions observed in the region with lower gas velocity. One possible source of discrepancy is the presence of an inactive void (trapped gas) in this region. Experimental evidence of such trapped gas was observed by Chu *et al.* (1983). Physically, an inactive void is a manifestation of the capillary force at the point of contact between adjacent particles. The amount of trapped gas is thus higher at smaller particle diameters due to increases in both capillary force and the number of contacts associated with smaller particles. Since Lee (1986) measured void fractions with a gamma densitometer, his measurements naturally include both active and inactive components of void fractions. As mentioned earlier, the present model does not include capillary pressure. Consequently, such trapped gas cannot be predicted in this work and void fractions obtained by the presence model should only be interpreted as the active component. Furthermore, the presence of an inactive void has a relatively minor influence on the porosity and permeability of the porous media and does not significantly affect the calculation of the active void here.

Figures 4(a–c) show the numerical solutions obtained for the case $D_{p_0} = 2.5$ mm, $D_{p_1} = 6$ mm, $H = 46$ cm, $J_G = 9.75$ mm/s and $J_L = 7.21$ mm/s. Since the region directly above the blockage is now occupied by a more permeable porous layer, the point of maximum gas velocity has been shifted slightly to the right of the centerline, as shown in figure 4(a). It is particularly interesting to note that, despite the blockage, most of the liquid now flows through the right half of the channel where permeability is the highest. The predicted pressure drop plotted in figure 4(b) displays behaviors very similar to those shown in figures 2(b) and 3(b). Again the void fractions shown in figures 4(c) agree quite favorably with Lee's (1986) data. For the same reason as cited earlier, the agreement between predicted and measured void fractions deteriorates in the region above the blockage where void fractions are small. It should also be pointed out that, in the region of higher gas velocity, the void fractions predicted in this case are higher than those shown in figure 3(c) due to an increase in drag forces. In fact, Lee (1986) found that such behavior cannot be predicted without the interfacial drag terms in the momentum equations.

3.2. One-dimensional Dryout With Volumetric Heating and Bottom Through Flow

As a check on the validity of the present physical models of drag forces, one-dimensional dryout in a volumetrically heated porous layer saturated with Freon-113 has been obtained with the present numerical scheme. The porous layers in this case are formed with heated particles of 3.2 and 4.8 mm dia. The height of the porous layers has been taken as 15 cm, corresponding to the experimental configurations employed by Tsai (1987). Liquid is injected into the porous layers at the bottom. At low liquid flow rates, only the lower portion of the porous layer experiences an upward flow of liquid, while the upper portion of the porous layer experiences a downward liquid flow. Dryout is then limited by counter-current flooding at the top of the porous layer. Even then, the liquid flow at the bottom results in a reduction of the liquid downflow at the top of the porous layer for any given volume heating rate and the dryout limit increases with increasing liquid inflow at the bottom. On the other hand, at higher liquid flow rates, only upward flow of liquid is present in the porous layer. As such, dryout is limited only by liquid starvation at the top of the porous layer and the asymptotic limit can be given by

$$q = \rho_L j_L h_{fg}. \qquad [38]$$

The dryout heat fluxes predicted from the present model are plotted in figure 5 as a function of the liquid mass flow rate. Also plotted in figure 5 are the experimental data obtained by Tsai (1987). It appears that the present model does well in predicting the dryout heat flux in most cases. It should be noted that the mechanistic models for drag forces proposed by Tung & Dhir (1988) have been used in this work without any modification. In light of the fact that their models were based on a set of data obtained with air–water mixtures, the results shown in figure 5 are surprisingly

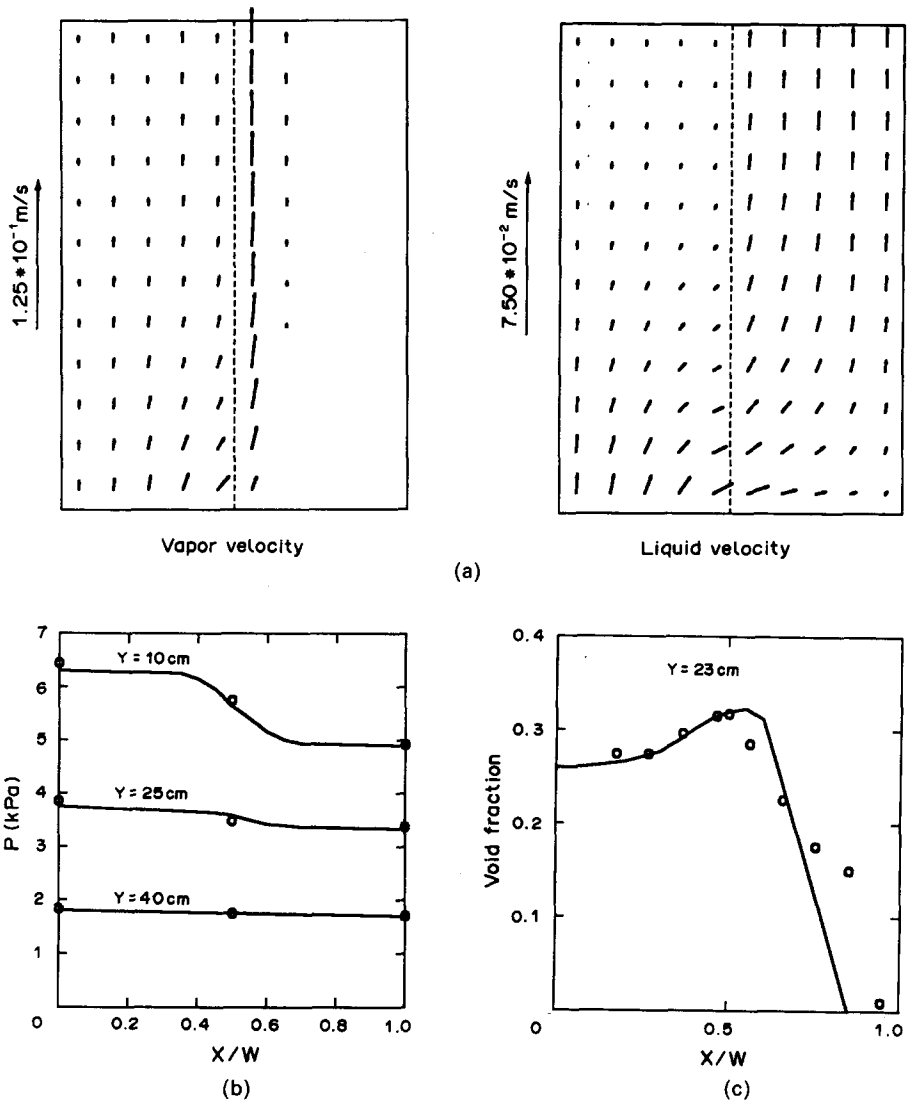

Figure 4. Two-dimensional solution with big particles above the blockage.

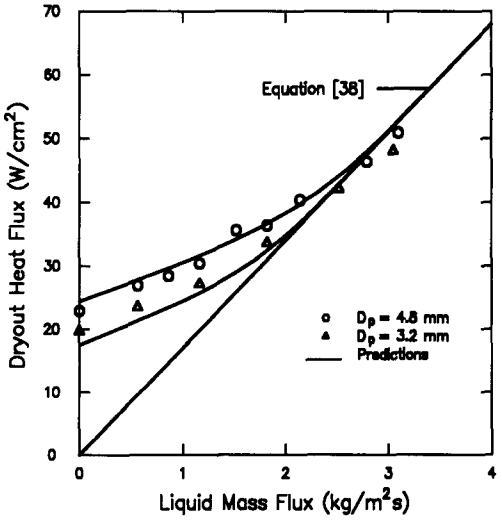

Figure 5. One-dimensional dryout with bottom liquid injection.

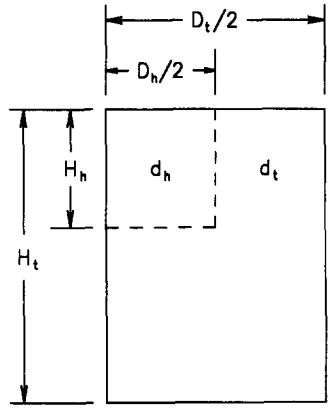

Figure 6. Axi-symmetric geometry with volumetric heating.

good. It should also be pointed out that the predicted dryout heat fluxes shown in figure 5 do indeed approach the asymptotic limit set forth in [38] regardless of particle size.

3.3. *Axi-symmetric Geometry With Volumetric Heating*

The present numerical scheme has also been employed to predict flow patterns in cases involving volumetric heating in axi-symmetric coordinates. Under consideration is a cylindrical region with diameter D_t and height H_t. Within this region, there is a subregion with diameter D_h and height H_h, as shown in figure 6. This subregion contains a volumetrically heated porous layer formed with particles of diameter d_h, while the surrounding region is formed with non-heated particles of diameter d_t. The porous layers are assumed to be flooded with saturated Freon-113 at 1 atm. Such a configuration corresponds approximately to the experimental configurations employed by Tsai (1987) in his measurements of dryout heat fluxes. Even though there was an overlying fluid layer above the porous media in Tsai's experiments, no specific information about this layer could be obtained in Tsai's (1987) work. Without this information one has little choice but to assume that an isobaric condition exists at the top of the domain. The effect of the overlying fluid layer, however, is expected to be of secondary importance and should not seriously impair the solutions. The outer boundaries of the non-heated region represent the container used in Tsai's experiments. Consequently, an impermeable boundary condition will be applied there. As discussed earlier in the analysis, no special treatment is required at the inner boundary between the heated region and the non-heated region.

Figure 7 shows flow patterns obtained with $D_t = 25$ cm, $H_t = 25$ cm, $d_t = 10$ mm, $D_h = 12.5$ cm, $H_h = 12.5$ cm, $d_h = 10$ mm and a relatively low volume heating rate ($Q = 8 \times 10^5$ W/m^3). It is interesting to note that the vapor flow is nearly one-dimensional in nature and is confined mostly to the heated region. This behavior is a manifestation of the dominance of the buoyancy force on

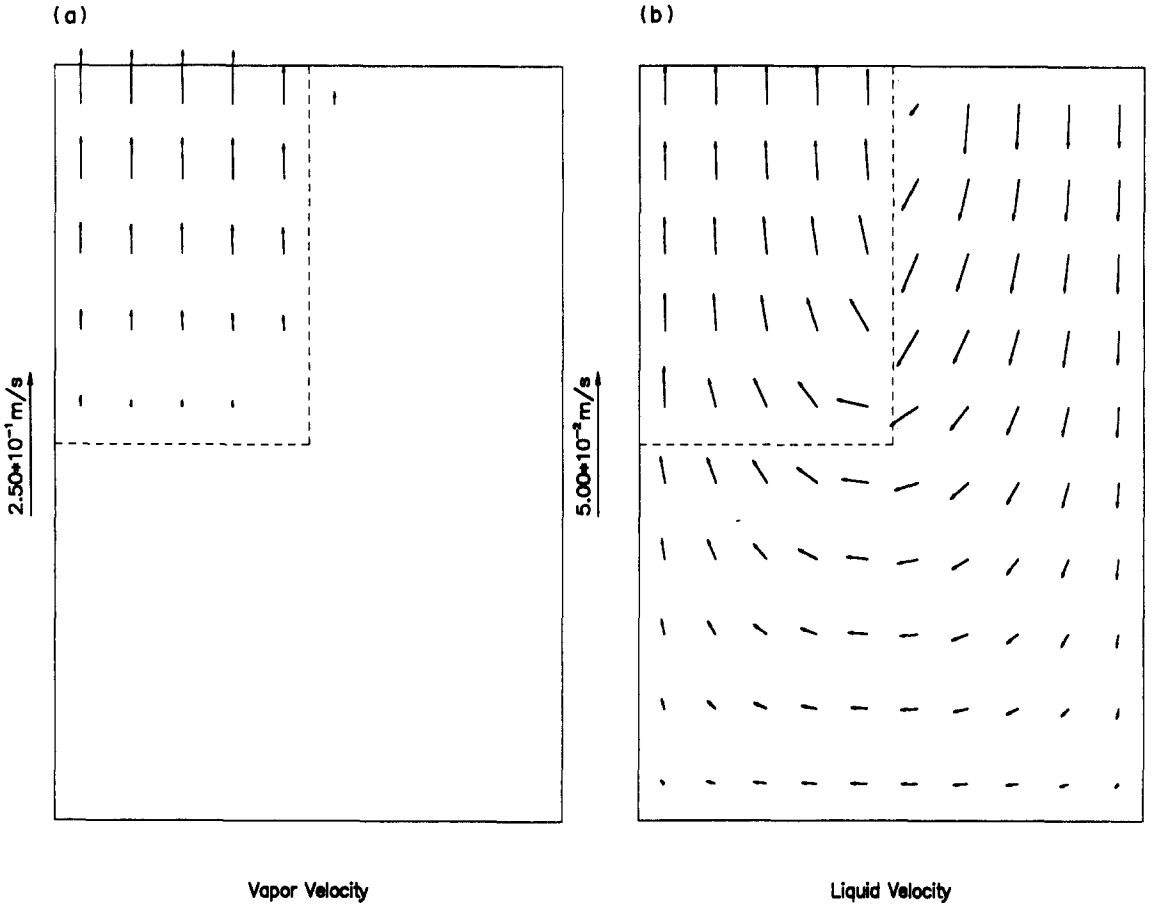

Figure 7. Axi-symmetric solution with volumetric heating—low heat generation.

the vapor phase compared to other drag forces. The presence of vapor flow in the heated zone causes an increase in the void fractions, resulting in a decrease in the hydrostatic pressure in this region. Another consequence of the vapor flow is an upward drag on the liquid in the heated region due to the interfacial term in the momentum equation. The pressure deficit, coupled with the upward drag on the liquid, is able to overcome gravity, resulting in an upward flow of liquid in the heated region. Mass conservation then requires that the liquid be fed into the heated zone through the boundary between the two regions, as shown in figure 7. Inside the heated region, the flow is thus mostly co-current, similar to the case of one-dimensional forced flow cooling. In the non-heated region, the liquid flow is mostly downward near the top of the domain to compensate for the upward liquid flow in the heated region. Dryout is thus expected to be caused by liquid starvation in the heated region rather than by counter-current flooding in this case.

Figure 8 shows flow patterns obtained at the point of dryout ($Q = 10^7$ W/m^3) for the same geometry. As the rate of volume heating increases, the increase in vapor velocity in the heated region results in higher friction. Eventually, the increase in friction will exceed the reduction in hydrostatic pressure caused by higher void fractions. As such, the pressure deficit discussed earlier may no longer exist and the liquid flow into the heated region will be seriously curtailed. The reduction in liquid flow is further compounded by an increase in the liquid sink (evaporation) associated with the higher volume heating rate. Eventually, evaporation overcomes the amount of liquid which can be fed into the heated region and dryout at the top of the bed due to liquid starvation will occur, as shown in figure 8. It should be noted further that the liquid downflow at the top of the non-heated region is also impeded by the pressure build up in the heated region and is much smaller than that shown in figure 7.

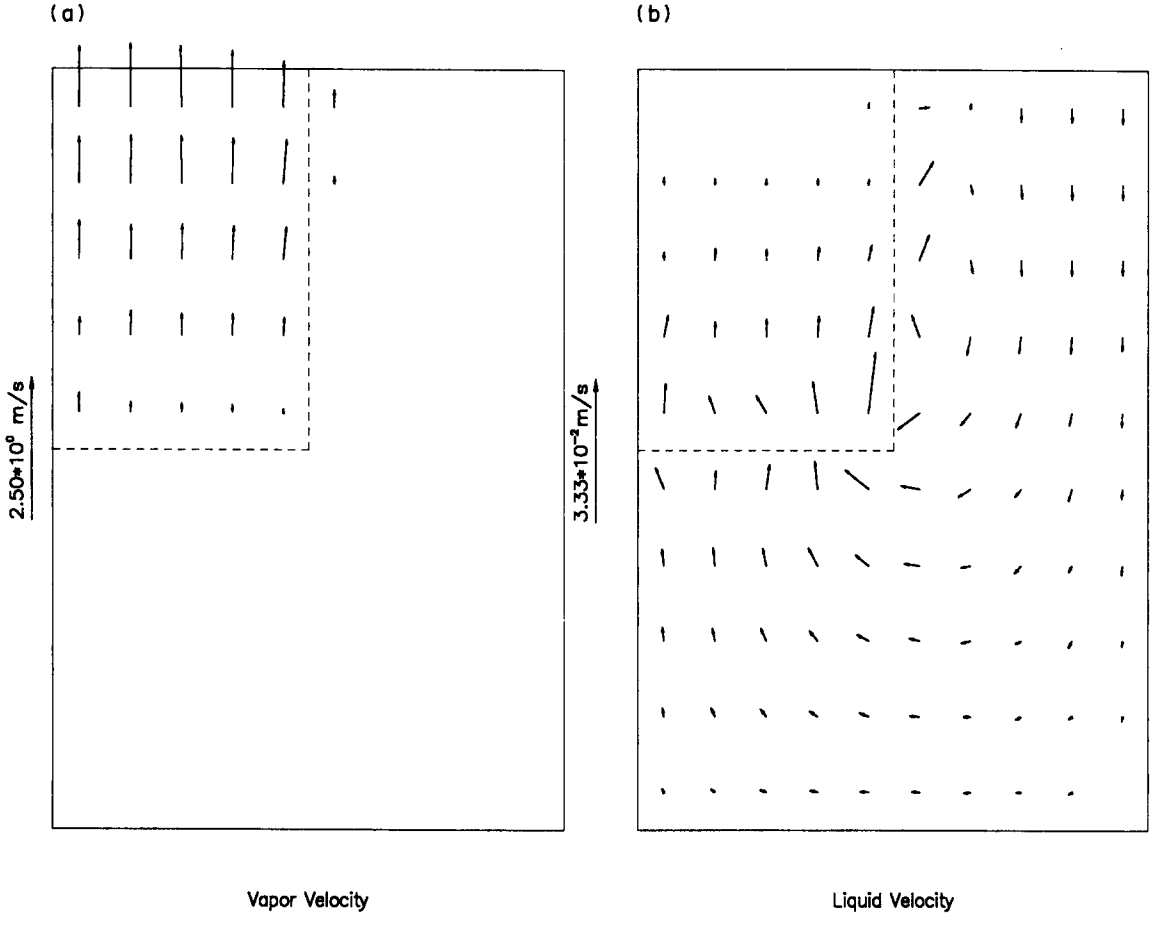

Figure 8. Axi-symmetric solution with volumetric heating—at the dryout condition.

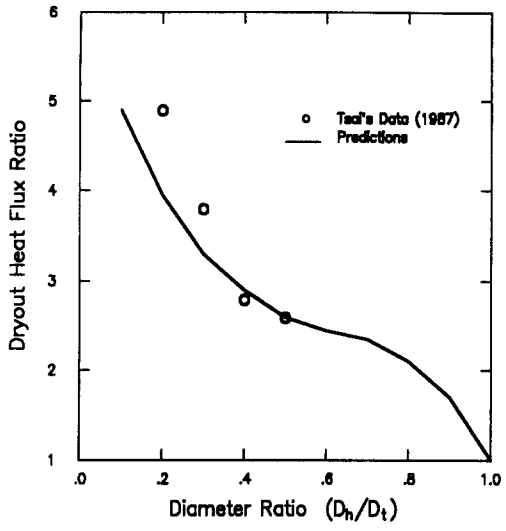

Figure 9. Dryout heat flux ratio with varying diameter ratio.

Figure 9 shows the dryout heat flux obtained with the present solution. The geometry used in the calculation corresponds to the experimental conditions employed by Tsai (1987) in his measurements—$D_t = 15$ cm, $H_t = 25$ cm, $d_t = 6$ mm, $H_h = 10$ cm, $d_h = 3.2$ mm and variable D_h. The scaled dryout heat flux is plotted in figure 9 as a function of the diameter ratio (D_h/D_t) between the heated and the non-heated regions. Scaling of the dryout heat flux is performed using the calculated one-dimensional value corresponding to the counter-current flooding limit (17.5 W/cm^2). In subsequent discussion, this scaled dryout heat flux will be referred to as the dryout ratio. A preliminary examination of figure 9 shows that the dryout ratio begins at a value of unity and increases monotonically as the diameter ratio decreases from unity. The sensitivity of the dryout ratio, however, appears to depend on the diameter ratio itself. This is indicative of a change in the limiting mechanism leading to dryout. Since departure from the counter-current flooding limit results partly from the liquid inflow at the bottom and partly from the inflow across the side of the heated region, an examination of the relative importance of the two flow paths is in order. The areas of the two possible liquid flow paths depend on the diameter of the heated region. The bottom area of the heated region varies like D_h^2 while the side area varies like $D_h H_h$. For a fixed height of the heated region, the ratio of the bottom area and the side area is thus proportional to the diameter ratio. As a result, the bottom flow is dominant at diameter ratios near unity, while the side flow is dominant at diameter ratios near zero. On the other hand, liquid must be available to the heated region regardless of the entry point. The flow area of the liquid near the top of the non-heated region thus represents another possible limitation on dryout heat fluxes. One then must closely examine the inter-dependence of these effects before arriving at any conclusions on the limiting mechanism of dryout.

3.3.1. Diameter ratio near unity ($D_h/D_t \approx 1$)

In this range of diameter ratio, bottom flow is dominant. However, such bottom flow is in turn restricted by liquid friction near the top of the non-heated region due to the restricted flow area there. With a slight reduction in the diameter ratio from unity, a flow channel is quickly established for the liquid downflow in the non-heated region. Liquid friction is thus drastically reduced and the dryout ratio increases rapidly as the diameter ratio is reduced from a value near unity.

3.3.2. Moderate diameter ratio

Once the flow channel for the liquid has been established in the non-heated region, liquid friction no longer controls the amount of liquid which arrives at the heated region. The dryout heat flux then is essentially controlled by a balance of the pressure drops in the heated and the non-heated channels with a relatively mild influence from the side flow. Consequently, the dryout ratio is relatively insensitive to the diameter ratio in this range.

3.3.3. *Diameter ratio near zero* ($D_h/D_t \approx 0$)

When the diameter ratio is near zero, the side flow becomes dominant and the dryout heat flux is mostly controlled by the amount of liquid available through the side of the heated region. The principal flow path for the liquid is thus very short and the dryout heat flux increases very quickly with decreasing diameter ratios. Theoretically, the dryout ratio must approach infinity as the diameter ratio approaches zero. Physically, however, the present solution may not be valid at very small diameter ratios since the averaging process used in deriving the drag forces is questionable for such short length scales in the heated region.

Also plotted in figure 9 are the dryout heat flux data obtained by Tsai for similar configurations. The agreement between Tsai's data and the present numerical solution appears to be fairly good despite the fact that the diameter ratio seems to influence the data slightly more than the predictions. This discrepancy, however, may be a result of the neglect of the overlying fluid layer in the present analysis. With the presence of such an overlying layer, the vapor plume above the heated region will result in higher pressure deficit between the two regions causing more liquid to be fed into the heated region than that predicted by the present analysis. Since the vapor plume is expected to spread out in the upward direction, this additional pressure deficit is higher at lower diameter ratios. As as result, the effect of the overlying layer should be more pronounced at smaller diameter ratios. This, in turn, results in a sharper variation of the dryout ratio. This effect is not included in the present solution since an isobaric condition has been imposed at the top of the porous layer as discussed earlier.

It should be mentioned here that the dryout heat fluxes shown in figure 9 were obtained by slowly increasing the volumetric heating rate until the liquid velocity at the top of the heated region vanished. The local void fraction at this point is usually within 0.1% of unity. Any further change in the heating rate cannot be sustained by the two-fluid model employed in this work since only the vapor phase would be present in the dry region. Furthermore, steam cooling was not considered in the present analysis as it required a complete solution of the energy equation as well as a switch from a two-fluid model to a single-phase model in the dry region.

Finally, a few comments must be made about the validity of the present solution regarding the size of the elements and that of the porous layers. Even though the models for the drags were obtained by an averaging process over a large volume, there is no reason the solution has to be carried out with huge elements. When a strong discontinuity exists, smaller elements must be used to capture the rapid change in void fraction and velocity near the discontinuity. The void fraction and velocity over a small element simply represent the average quantity at that point if one expands the surrounding averaging volume indefinitely around that particular point in space. In fact, from this point of view, the porous medium can be treated as a continuum. On the other hand, the total volume of the porous medium must be large enough so that an expansion of the averaging volume around any point in the domain is meaningful or the solution will not bear physical sense.

4. CONCLUSIONS

Numerical solutions of the two-phase momentum and continuity equations in a volumetrically heated porous layer are sought through the use of the FEM. The numerical scheme allows a domain to contain several regions of distinct permeabilities and volume heating rates. Along the exterior boundaries either pressure or fluid fluxes must be specified.

Solutions obtained for two-phase flow in a two-dimensional channel with blockage and stratification are in good agreement with experimental data reported in the literature.

Dryout heat fluxes obtained in one-dimensional volumetrically heated porous layers with liquid through flow at the bottom are in good agreement with existing experimental data. At low liquid flow rates, dryout is limited by counter-current flooding limit at the top of the porous layer. At higher flow rates, liquid starvation at the top of the porous layers appears to control the dryout heat fluxes.

Solutions obtained for an axi-symmetric channel with partial volume heating indicate that the vapor flow pattern is basically one-dimensional within the confinement of the heated region. The liquid, however, is found to be fed into the heated region through both the side and bottom of the heated zone.

Dryout with partial volume heating is found to occur via a mechanism similar to that of bottom flooding and is much higher than the corresponding counter-current flooding limit. The dryout heat flux can be satisfactorily predicted by the present analysis. However, better results can be obtained if the overlying liquid layer is also taken into account.

REFERENCES

CHU, W., DHIR, V. K. & MARSHALL, J. S. 1983 Study of pressure drops, void fraction and relative permeabilities of two-phase flow through porous media. *AIChE Symp. Ser.* **79**(225), 224–235.

HILDEBRAND, B. F. 1975 *Methods of Applied Mathematics*, 2nd edn. Prentice-Hall, Englewood Cliffs, N.J.

LEE, H. S. 1986 Two phase flow through porous media. Ph.D. Dissertation, Univ. of California, Los Angeles.

SCHULENBERG, T. & MULLER, U. 1984 A refined model for the coolability of core debris with flow entry from the bottom. Presented at the *6th Information Exchange Mtg on Debris Coolability*, Univ. of California, Los Angeles.

SEGERLIND, J. L. 1976 *Applied Finite Element Analysis*. Wiley, New York.

TSAI, F. P. 1987 Dryout heat flux in a volumetrically heated porous bed. Ph.D. Dissertation, Univ. of California, Los Angeles.

TUNG, V. X. 1988 Hydrodynamic and thermal aspects of two phase flow through porous media. Ph.D. Dissertation, Univ. of California, Los Angeles.

TUNG, V. X. & DHIR, V. K. 1988 A hydrodynamic model for two-phase flow through porous media. *Int. J. Multiphase Flow* **14**, 47–65.

TUTU, N. K., GINSBERG, T. & CHEN, J. C. 1983 Interfacial drag for two-phase flow through high permeability porous beds. Presented at the *21st natn. Heat Transfer Conf.*, Seattle, Wash.

WYLIE, R. C. 1975 *Advanced Engineering Mathematics*, 4th edn. McGraw-Hill, New York.

APPENDIX

The drag coefficients and relative permeability multipliers proposed by Tung & Dhir (1988) are summarized in this appendix. These coefficients are currently used in the calculation of drag forces shown in [4]–[6].

Bubble Diameter

For porous layers composed of large diameter particles, the bubble diameter is controlled by surface tension and buoyancy and is given by

$$D_b = 1.35\left[\frac{\delta}{g(\rho_L - \rho_G)}\right]^{1/2}. \qquad [A.1]$$

However, with smaller particle diameters, the pore space is too small to accommodate such big bubbles and the bubble diameter must be given by

$$D_b = \frac{\alpha}{1-\alpha} D_p \qquad [A.2]$$

Once the bubble diameter has been found, the diameter ratio between bubbles and particles can be calculated as

$$\gamma = \frac{D_b}{D_p}. \qquad [A.3]$$

Flow Regimes

Bubbly flow

The bubbly flow regime can be divided into two subregimes ($\epsilon \leqslant \epsilon_0$) and ($\epsilon_0 \leqslant \epsilon \leqslant \epsilon_1$), where ϵ_0

and ϵ_1 are given by

$$\epsilon_0 = \frac{\pi}{3}\frac{1-\alpha}{\alpha}\gamma(1+\gamma)[6\eta - 5(1+\gamma)] \qquad \text{as long as } \epsilon_0 \geqslant 0 \qquad [A.4]$$

and

$$\epsilon_1 = 0.6(1-\gamma^2) \qquad \text{as long as } \epsilon_1 \geqslant 0.3; \qquad [A.5]$$

$$\eta = \left[\frac{\pi\sqrt{2}}{6(1-\alpha)}\right]^{1/3} \qquad [A.6]$$

Slug flow

Pure slug flow occurs in the range of $(\epsilon_2 \leqslant \epsilon \leqslant \epsilon_3)$, where ϵ_2 and ϵ_3 are given by

$$\epsilon_2 = \frac{\pi}{6} \qquad [A.7]$$

and

$$\epsilon_3 = 0.6. \qquad [A.8]$$

Annular flow

Pure annular flow is assumed to occur in the range of $(\epsilon_4 \leqslant \epsilon \leqslant 1)$, where ϵ_4 is given by

$$\epsilon_4 = \frac{\pi\sqrt{2}}{6}. \qquad [A.9]$$

Liquid Relative Permeability Multipliers

For all flow regimes, the liquid relative permeability multipliers are given by

$$\kappa'_L = \eta'_L = (1-\epsilon)^3. \qquad [A.10]$$

Gas Relative Permeability Multipliers

Bubbly and slug flow $(\epsilon \leqslant \epsilon_3)$

$$\kappa'_G = \left(\frac{1-\alpha}{1-\alpha\epsilon}\right)^{4/3}\epsilon^3 \quad \text{and} \quad \eta'_G = \left(\frac{1-\alpha}{1-\alpha\epsilon}\right)^{2/3}\epsilon^3. \qquad [A.11]$$

Annular flow $(\epsilon_4 \leqslant \epsilon \leqslant 1)$

$$\kappa'_G = \left(\frac{1-\alpha}{1-\alpha\epsilon}\right)^{4/3}\epsilon^2 \quad \text{and} \quad \eta'_G = \left(\frac{1-\alpha}{1-\alpha\epsilon}\right)^{2/3}\epsilon^2. \qquad [A.12]$$

Interfacial Drag Coefficients C'_i and C'_t

Bubbly flow $(\epsilon \leqslant \epsilon_1)$

(i) $\epsilon \leqslant \epsilon_0$,

$$C'_v = 18\epsilon f \quad \text{and} \quad C'_i = 0.34(1-\epsilon)^3\epsilon f^2; \qquad [A.13]$$

(ii) $\epsilon_0 \leqslant \epsilon \leqslant \epsilon_1$,

$$C'_v = 18(\epsilon_0 f + \epsilon - \epsilon_0) \quad \text{and} \quad C'_i = 0.34(1-\epsilon)^3(\epsilon_0 f^2 + \epsilon - \epsilon_0); \qquad [A.14]$$

$$f = \tfrac{1}{2}(1+\gamma)\log_e\left(1+\frac{2}{\gamma}\right). \qquad [A.15]$$

Slug flow $(\epsilon_2 \leqslant \epsilon \leqslant \epsilon_3)$

$$C'_v = 5.21\epsilon \quad \text{and} \quad C'_i = 0.92(1-\epsilon)^3\epsilon. \qquad [A.16]$$

Annular flow ($\epsilon_a \leqslant \epsilon \leqslant 1$)

$$C'_v = \frac{a^* \mu_G}{\kappa'_G} \times \frac{g D_b^2 (1 - \rho^*)\alpha}{\nu_L} \qquad [A.17]$$

and

$$C'_i = \frac{\epsilon}{1 - \epsilon} \times \frac{b^* \rho_G}{\eta'_G} \times \frac{g D_b (1 - \rho^*)\alpha^2}{1 - \epsilon + \rho^* \epsilon}, \qquad [A.18]$$

where the relative permeabilities multipliers κ'_G and η'_G are given by [A.12], while a^* and b^* are given by [8].

It should be noted that the above coefficients are applicable only in the pure bubbly flow, pure slug flow and pure annular flow regimes. In the transition flow regimes, one must apply a weighting factor between the two adjacent regimes. In the present work, a smooth transition between two flow regimes a and b is provided by a weighting factor W such that any drag coefficient C is given by

$$C = C_a(1 - W) + C_b W, \qquad [A.19]$$

where C_a and C_b are the coefficients evaluated in the flow regimes a and b, respectively.

The weighting factor W varies between zero and unity and is obtained by

$$W = \zeta^3(10 - 15\zeta + 6\zeta^2), \qquad [A.20]$$

where

$$\zeta = \frac{(\epsilon - \epsilon_a)}{(\epsilon_b - \epsilon_a)}. \qquad [A.21]$$

Such a weighting factor has been chosen such that the first and second derivatives of C with respect to ϵ are continuous at the end points ϵ_a and ϵ_b.